Estimating Ion Escape from Unmagnetized Planets

Mats Holmstrom

Swedish Institute of Space Physics, PO Box 812, SE-981 28 Kiruna, Sweden

Correspondence: Mats Holmstrom (matsh@irf.se)

Abstract. We propose a new method to estimate ion escape from unmagnetized planets that combines observations and models. Assuming that upstream solar wind conditions are known, a computer model of the interaction between the solar wind and the planet is executed for different ionospheric ion production rates. This results in different amounts of mass loading of the solar wind. Then we obtain the ion escape rate from the model run that best fit observations of the bow shock location. As an example of the method we estimate the heavy ion escape from Mars on 2015-03-01 to be $2 \cdot 10^{24}$ ions per second, using a hybrid plasma model and observations by MAVEN and Mars Express. This method enables studies of how escape depend on different parameters, and also escape rates during extreme solar wind conditions, applicable to studies of escape in the early solar system, and at exoplanets.

1 Introduction

Ion escape to space is important for the evolution of planetary atmospheres. Neutrals in the upper parts of the atmosphere can be ionized by, e.g., UV photons, charge exchange, and electron impacts. The newly created ion can then be energized by electric fields and transported away by the stellar wind, overcoming gravity, resulting in atmospheric loss.

For planets in our solar system, we can observe the present day escape of planetary ions by directly observing the ion flux near a planet. This is done using an ion detector on a spacecraft and gives us the flux of ions along the trajectory of the spacecraft. Since the flux of escaping ions is highly variable in time and location, accurately estimating the escape of ions can require observations over many years to get an average escape rate. To investigate how the escape rate of ions depend on different parameters, e.g., upstream solar wind conditions, is even more difficult due to the large amounts of observations needed to get sufficient statistics.

Another way to estimate ion escape rates is to use computer models of the solar wind interaction with a planet. An advantage of models compared to observations is that we at every instance get the full three-dimensional escape. In addition, there are no limitations in sensitivity, energy range or field of view as there is for observations. However, to accurately estimate ion escape requires that the model contains all important physical processes, in sufficient detail. It is questionable if this is the case at present.

Here we propose an alternative method of estimating ion escape. A method that uses both observations and computer models. Instead of directly observing the escaping ions, we use observations of other plasma quantities near the planet. Then we use a

parameterized model and find the set of model parameters that give the best fit between the model and the observations. The model escape rate for the best fit parameters then gives us an estimate of the ion escape rate.

This approach allow us to use data sets traditionally not used for ion escape estimates, e.g., magnetic field and electron observations. We can also estimate the escape rate from a very small set of observations, during one orbit of a space craft around a planet, or during one flyby of a planet.

To illustrate this general method we estimate the escape rate of ions from Mars during one bow shock crossing of the MAVEN spacecraft (Jakosky et al., 2015) using magnetic field observations of the bow shock location, observations of the upstream solar wind conditions, and a hybrid plasma model. We also use Mars Express (MEX) (Barabash et al., 2007) observations of electrons to verify our findings.

The location and shape of the Martian bow shock has been the topic of many observational studies. Where is the bow shock located, and what are the controlling parameters? Recently Hall et al. (2016) found a seasonal dependence of the bow shock location, and later also a solar cycle dependence (Hall et al., 2019). The seasonal dependence should be due to the changing distance from the Sun of Mars. It is not straight forward to deduce if it is due to changing solar wind pressure or changing EUV insolation, since both scale in the same way with distance from the Sun. Also, both the solar wind and the EUV insolation changes over a solar cycle. Regarding the effect of crustal magnetic fields on the bow shock location, Gruesbeck et al. (2018) find such a dependence, and a modeling study by Fang et al. (2017) finds that a large part of the variability in escape may be due to the crustal fields, reducing and enhancing escape, depending on the location. Regarding the shape of the bow shock, Vignes et al. (2002) found that it is furthest away from the planet in the hemisphere in the direction of the solar wind convective electric field.

However, it has been noted that, apart from the upstream solar wind conditions, the factor controlling the location of the shock is the amount of mass loading of the solar wind by ionospheric ions. This was noted for Venus by Alexander and Russell (1985), and later for Mars by Vignes et al. (2002) and Mazelle et al. (2004). The EUV flux, atmospheric state, ionospheric chemistry, magnetic anomalies, and similar factors will all affect the location of the bow shock, but only indirectly through the amount of mass loading. Therefore, given upstream solar wind conditions, we should be able to use the amount of mass loading as a free parameter when modeling the location of the bow shock.

2 Method

The algorithm presented in this paper is general, and can be applied to any model of the interaction between Mars and the solar wind. To illustrate the method we here use a very simple hybrid model.

We now describe the hybrid plasma solver used, the adaptation for Mars, the parameters used; the observations of magnetic field, ions and electrons used, and finally the algorithm to estimate ionospheric ion escape.

2.1 Hybrid model

In the hybrid approximation, ions are treated as particles, and electrons as a massless fluid. The trajectories of the ions are computed from the Lorentz force, given the electric and the magnetic fields. The electric field is

$$\mathbf{E} = \frac{1}{\rho_I}\left(-\mathbf{J}_I \times \mathbf{B} + \mathbf{J} \times \mathbf{B} - \nabla p_e\right) + \eta \mathbf{J}, \tag{1}$$

where ρ_I is the ion charge density, $\mathbf{J}_I$ is the ion current density, p_e is the electron pressure, and η is the resistivity. The current is computed from, $\mathbf{J} = \mu_0^{-1} \nabla \times \mathbf{B}$, where $\mu_0 = 4\pi \cdot 10^{-7}$ is the magnetic constant.

Then Faraday's law is used to advance the magnetic field in time,

$$\frac{\partial \mathbf{B}}{\partial t} = -\nabla \times \mathbf{E}.$$

Further details on the hybrid model used here, the discretization, and the handling of vacuum regions can be found in Holmstrom et al. (2012).

2.2 Mars model

In the hybrid simulation domain, Mars is modeled as a resistive sphere, of radius R, centered at the origin, where all ions that hit the obstacle are removed from the simulation.

The ionosphere is represented by the production of a single specie of ions according to an analytical Chapman ionospheric profile (Holmstrom and Wang, 2015), where the production rate of ions is given by

$$P(h, \chi) = p e^{1 - y - \sec \chi e^{-y}}, \qquad y = (h - h_0)/H, \qquad h \geq 0, \quad 0 \leq \chi < \pi/2, \tag{2}$$

where h [m] is the height above the planet surface, χ [rad] is the solar zenith angle (SZA), p [$\mathrm{m^{-3}s^{-1}}$] is the maximum production along the sub-solar line, at height h_0 [m], and H [m] is the scale height. Ions are then randomly placed according to this production function, and also given a random thermal velocity corresponding to a temperature of 200 K.

We note that the ion production is a free parameter in such a model. This is in contrast to models that self consistently include ionospheric chemistry and a neutral atmosphere (Brecht et al., 2016). Usually this free parameter is seen as a limitation of the model, but here we use this as an advantage, to find a best fit to observations. This means that it is not important what the exact processes are in the ionosphere that produce the ions, or how they are transported to the top of the ionosphere.

Regarding the composition of escaping ionospheric ions. A study by Carlsson et al. (2006) based on Mars Express observations found flux ratios of O_2^+/O^+ = 0.9 and CO_2^+/O^+ = 0.2. Later Rojas-Castillo et al. (2019) estimated that O_2^+/O^+ = 0.76. Using MAVEN data, Inui et al. (2019) found a flux ratio of O_2^+/O^+ = 1.2, and that CO_2^+ contributed less than 10% to the total heavy ion flux. In summary, observations indicate that the flux of escaping O^+ and O_2^+ ions are of similar magnitude, while the CO_2^+ flux is not significant.

Since the code used here only handles one single-charged ionospheric ion specie, we make separate simulation runs using O^+ and O_2^+ to investigate the effects of composition on the ion escape rate estimates. Note also that there is no neutral H

or O corona in the model. So those populations of exospheric pick-up ions are missing. That means the mass loading due to the corona is missing in the simplified model we use. The total mass loading can be compensated by more ions from the ionospheric source, but in reality the spatial distribution would be different. We also do not include any alpha particles in the solar wind, that should have some effect on the solar wind interaction.

2.3 Model parameters

The coordinate system used is MSO coordinates with the solar wind flowing along the $-x$-axis, with density n_{sw}, speed v_{sw} and temperature T_{sw}. The upstream interplanetary magnetic field is $\mathbf{B}_{sw}$. The computational grid has cubic cells of size Δx and the time step is Δt. The computational domain is $-11000 \leq x \leq 10000$, $-33600 \leq y, z \leq 33600$ km. On the upstream boundary, after each timestep, we insert solar wind protons so that the number of particles per cell there is constant. In the y and z directions we have periodic boundary conditions. The produced ionospheric ions have a weight (how many real ions they represent) that is chosen such that the weight is similar to that of the solar wind protons. The model parameters and their values are listed in Table 1.

2.4 Observations

We use MAVEN magnetic field (Connerney et al., 2015) and ion (Halekas et al., 2017) observations to determine upstream conditions and bow shock location. The orbit is chosen such that the solar wind conditions are steady, so that the conditions should be unchanged while MAVEN is inside the bow shock, when we do not have observations of the solar wind. This also allow us to use a simulation that does not have time dependent upstream solar wind conditions. To verify our results we also use Mars Express (MEX) observations of electrons (Frahm et al., 2006) to locate bow shock crossings. The upstream solar wind parameters are listed in Table 1.

2.5 Algorithm

Now we describe the algorithm for estimating the escape of ionospheric ions from observations of the upstream solar wind and the location of the bow shock. The algorithm is illustrated in Fig. 1.

1. We start with an observed state of the upstream solar wind: The magnetic field; the solar wind density, velocity and temperature.
2. Then we make several runs of the hybrid model for these upstream solar wind conditions, using different ionospheric ion production rates.
3. We then find the simulation run that has a bow shock location that best correspond to the observed location. This could be done quantitatively, e.g., by a least square fit, but here we visually compare the simulations and the observations.
4. The escape for the best fit simulation run is then computed and this will be our estimate of the escape rate of ionospheric ions at the time of the bow shock observation.

3 Results

As an example of the proposed algorithm we performed ten simulations with the production rates $p_i = 0.1, 0.2, \ldots, 1.0$ [cm^{-3}s^{-1}]. In Fig. 2 we present a comparison of MAVEN observations and two hybrid runs (R_1 and R_2) with an O^+ ionosphere and different ion production rates that were judged to best fit the observations. We see that there is a fairly good agreement between the models and the observations at the bow shock and in the magnetosheath. Closer to the planet, in the induced magnetosphere, the agreement is however not so good. The magnetic field is much larger and more variable than in the model. This is not surprising since we have a model with a very simplified ionosphere, no magnetic anomalies, and low spatial resolution. Also, in the magnetosphere the proton velocities in the model are much higher than observed. However, the proton density is very small, close to zero, in much of this region both as observed and in the simulations. Near the exit from the induced magnetosphere the observed density is larger than in the simulations, resulting in a similar dynamic pressure. Also, the variability of B_z in the magnetosheath is smaller in the models than observed.

As expected, and seen when comparing the two model runs, the location of the bow shock moves outward when the ionospheric ion production is increased, resulting in a larger mass loading.

The escape rate never reach a steady state due to the intrinsic variability of the induced magnetosphere. So, we determine the escape rate by averaging the flux of ionospheric ions along $-x$ in the simulation domain, from $x = -5000$ km to the outflow boundary. We then average these computed escape values over time, between 200 s and 590 s, with a time step of 10 s.

In Table 2 we show the results of simulation runs R_1-R_4, performed for O^+ and O_2^+ ionospheres with different ion production rates. For the best fit runs using O^+ the approximate escape rate is $2.0 \cdot 10^{24}$, while it is $1.5 \cdot 10^{24}$ s^{-1} for O_2^+. Since in reality we have a mixture of the two ion species, the escape rate should be between these values, and we can estimate the actual escape as $2 \cdot 10^{24}$ s^{-1}.

We can note how the escape rate for the best fit simulation runs depends on the specie of the escaping ionospheric ions. The best fit has 25% less escaping O_2^+ ions compared to O^+. It is not however directly proportional to the total mass of the escaping ions, in that case we would expect a 50% reduction. So it is not only the amount of mass loading that characterize the best fit, the dynamics of the escaping ions is also important.

Looking at the escape in Table 2 for the same specie, but for different ion production rates, we see that the escape rate is weakly dependent on the production rate. The two best fit runs in Fig. 2 has less than 1% difference in escape rate.

To verify the location of the bow shock in the two best fit model runs, we also use Mars Express observations of the bow shock in electron data. In Fig. 3 we plot the proton number density from the same two hybrid runs as in Fig. 2, but now along the Mars Express orbit, together with the location of the bow shock crossings observed by MEX. The agreement is fairly good, even if the observed bow shock is a few minutes earlier than seen in the model runs. This corresponds to a distance of a few hundred kilometer, comparable to the simulation grid cell size. One reason for this could be that we have not used an aberrated solar wind velocity (it flows along the $-x$ axis). This should result in a tilt of the whole magnetosphere and bow shock.

4 Discussion

For our example case we found an escape rate of $2 \cdot 10^{24}$ ions per second. This is in the range of recently published estimates for the escape rate at Mars (Ramstad et al., 2015; Brain et al., 2015; Dong et al., 2017).

An assumption is that, given upstream condition, the mass loading determines the bow shock location. Although we find an escape rate for a single orbit that match observed escape rates, this assumption needs to be tested in more detail. An ongoing investigation is to apply the method to a large number of orbits and verify that the model estimated escape rates are consistent with observed escape rates.

The proposed method is directly applicable to unmagnetized planets. For magnetized planets the bow shock location is mainly determined by the upstream solar wind and the strength of the dipole field. Escape at magnetized planets occur in the cusp regions, and how that affects the bow shock location, and if the presented method could be adapted to magnetized planets would need further investigation.

The bow shock location has been found to depend on the location of the magnetic anomalies relative to the solar wind flow (Fang et al., 2017). Is it because the fields "push out" the boundaries, or because the fields increase ion escape? The latter may not require crustal fields in the model used in our algorithm. Since the parameter we vary is the amount of ions near Mars that is available to escape. If the crustal fields in a specific geometry enhance escape, this will be captured in the algorithm since the best fit bow shock will be further out, and if it depress escape the bow shock will be closer to the planet.

We used a hybrid plasma model in the algorithm. It would however be possible to use another type of plasma model, e.g., a magnetohydrodynamic (MHD) model, that can predict the location of the bow shock for different amounts of mass loading by ionospheric ions, given upstream solar wind conditions.

5 Conclusions

In the past, ion escape has been estimated either by computer models or from observations. Models have the problem that every physical process has to be present in the model. Observations suffer from variability, requiring the averaging of data over years, or even decades. The method proposed here uses a model and observations together. In that way we overcome the difficulties of each approach. We then get an estimate of the escape using just one observation. A model is used to estimate a global property (ion escape) from a local observation (bow shock location). Since we use a model, there are no physical limitations in terms of energy coverage and field of view that observations have. In particular low energy escaping ions are difficult to observe.

This opens up the possibility of estimating escape during flybys of unmagnetized planets, in the past and in the future. It also allow for estimating escape twice per orbit given only a magnetometer and an ion detector. This enables detailed studies of how the escape depends on different parameters. Something that has been difficult in the past due to the years of observations needed to collect enough statistics. It also makes possible the study of escape during transient events, like extreme solar wind conditions, something that is important for studies of escape in the past, and the escape at exoplanets.

Data availability. The MAVEN data used in this work, ion data from the SWIA instrument and magnetic field data from the MAG instrument, is available in NASA's Planetary Data System (PDS) at `https://pds-ppi.igpp.ucla.edu/search/view/?f=null&id=pds://PPI/maven.insitu.calibrated/data/2015/03`

The ASPERA-3 electron data used, from the ELS sensor, is available at `https://pds-ppi.igpp.ucla.edu/search/view/?id=pds://PPI/MEX-M-ASPERA3-3-RDR-ELS-EXT5-V1.0`

Author contributions. The author did all of the work.

Competing interests. The author declare that he has no conflict of interest.

Acknowledgements. Computing resources used in this work were provided by the Swedish National Infrastructure for Computing (SNIC) at the High Performance Computing Center North (HPC2N), Umeå University, Sweden. The software used in this work was in part developed by the DOE NNSA-ASC OASCR Flash Center at the University of Chicago.

References

Alexander, C.J., and C.T Russell (1985), Solar Cycle Dependence of the Location of the Venus Bow Shock, *Geophysical Research Letters*, v. 12, n. 6, 369–371. https://doi.org/10.1029/GL012i006p00369

Barabash, S., R. Lundin, H. Andersson, K. Brinkfeldt, A. Grigoriev, H. Gunell, et al. (2007), The Analyzer of Space Plasmas and Energetic Atoms (ASPERA-3) for the Mars Express mission, *Space Sci. Rev.*, 126(1–4), 113–164. https://doi.org/10.1007/s11214-006-9124-8

Brain, D. A., J.P. McFadden, J.S. Halekas, J.E.P. Connerney, S.W. Bougher, S. Curry, C.F. Dong et al. (2015), The spatial distribution of planetary ion fluxes near Mars observed by MAVEN, *Geophysical Research Letters*, 42, 9142–9148. https://doi.org/10.1002/2015GL065293

Brecht, S.H., S.A. Ledvina, and S.W. Bougher (2016), Ionospheric loss from Mars as predicted by hybrid particle simulations, *Journal of Geophysical Research: Space Physics*, 121, 10, 190–10. https://doi.org/10.1002/2016JA022548

Carlsson, E., A. Fedorov, S. Barabash, E. Budnik, A. Grigoriev, H. Gunell, et al. (2006), Mass composition of the escaping plasma at Mars, *Icarus*, 182(2):320–328. https://doi.org/10.1016/j.icarus.2005.09.020

Connerney, J.E.P., J.R. Espley, G.A. DiBraccio, J.R. Gruesbeck, R.J. Oliversen, D.L. Mitchell, et al. (2015), First results of the MAVEN magnetic field investigation, *Geophys. Res. Lett.*, 42, 8819–8827. https://doi.org/10.1002/2015GL065366

Dong, Y., X. Fang, D.A. Brain, J.P. McFadden, J.S. Halekas, J.E.P. Connerney, et al. (2017), Seasonal variability of Martian ion escape through the plume and tail from MAVEN observations, *Journal of Geophysical Research: Space Physics*, 122. doi:10.1002/2016JA023517

Fang, Xiaohua, Yingjuan Ma, Kei Masunaga, Yaxue Dong, David Brain, Jasper Halekas, et al. (2017), The Mars crustal magnetic field control of plasma boundary locations and atmospheric loss: MHD prediction and comparison with MAVEN, *Journal of Geophysical Research: Space Physics*, 122. doi:10.1002/2016JA023509.

Frahm, R.A., J.D. Winningham, J.R. Sharber, J.R. Scherrer, S.J. Jeffers, A.J. Coates, et al. (2006), Carbon dioxide photoelectron energy peaks at Mars, *Icarus*, 182, 2, 371–382. https://doi.org/10.1016/j.icarus.2006.01.014

Gruesbeck, Jacob R., Jared R. Espley, John E.P. Connerney, Gina A. DiBraccio, Yasir I. Soobiah, David Brain, et al. (2018), The Three-Dimensional Bow Shock of Mars as Observed by MAVEN, *Journal of Geophysical Research: Space Physics*, 123. https://doi.org/10.1029/2018JA025366

Halekas, J.S., S. Ruhunusiri, Y. Harada, G. Collinson, D. L. Mitchell, C. Mazelle, et al. (2017), Structure, dynamics, and seasonal variability of the Mars-solar wind interaction: MAVEN solar wind ion Analyzer in-flight performance and science results, *J. Geophys. Res. Space Physics*, 122, 547–578. https://doi.org/10.1002/2016JA023167

Hall, B.E.S., M. Lester, B. Sánchez-Cano, J.D. Nichols, D.J. Andrews, N.J.T. Edberg, et al. (2016), Annual variations in the Martian bow shock location as observed by the Mars Express mission, *Journal of Geophysical Research: Space Physics*, 121, 11,474–11,494. doi:10.1002/2016JA023316

Hall, B.E.S., B. Sánchez-Cano, J.A. Wild, M. Lester, and M. Holmström (2019), The Martian Bow Shock Over Solar Cycle 23-24 as Observed by the Mars Express Mission, *Journal of Geophysical Research: Space Physics*, 124, 4761–4772. https://doi.org/10.1029/2018JA026404

Holmström, M., S. Fatemi, Y. Futaana, and H. Nilsson (2012), The interaction between the Moon and the solar wind, *Earth Planets Space*, 64(2):237–245. doi:10.5047/eps.2011.06.040

Holmstrom, Mats, and Xiao-Dong Wang (2015), Mars as a comet: Solar wind interaction on a large scale, *Planetary and Space Science*, 119, 43–47. https://doi.org/10.1016/j.pss.2015.09.017

Inui, S., K. Seki, S. Sakai, D.A. Brain, T. Hara, J.P. McFadden, et al. (2019), Statistical Study of Heavy Ion Outflows From Mars Observed in the Martian-Induced Magnetotail by MAVEN, *Journal of Geophysical Research: Space Physics*, Volume 124, Issue 7, pp. 5482–5497. https://doi.org/10.1029/2018JA026452

Jakosky, B. M., J. M. Grebowsky, J. G. Luhmann, and D. A. Brain (2015), Initial results from the MAVEN mission to Mars, *Geophys. Res. Lett.*, 42, 8791–8802. https://doi.org/10.1002/2015GL065271

Mazelle, C., D. Winterhalter, K. Sauer, J.G. Trotignon, M.H. Acuña, K. Baumgärtel, et al. (2004), Bow Shock and Upstream Phenomena at Mars, *Space Science Reviews* 111, 115–181. https://doi.org/10.1023/B:SPAC.0000032717.98679.d0

Ramstad, R., S. Barabash, Y. Futaana, H. Nilsson, X.-D. Wang, and M. Holmström (2015), The Martian atmospheric ion escape rate dependence on solar wind and solar EUV conditions: 1. Seven years of Mars Express observations, *Journal of Geophysical Research: Planets*, 120, 1298–1309. https://doi.org/10.1002/2015JE004816

Rojas-Castillo, D., H. Nilsson, and G. Stenberg Wieser (2019), Mass Composition of the Escaping Flux at Mars: MEX Observations, *Journal of Geophysical Research: Space Physics*, Volume 123, Issue 10, pp. 8806–8822. https://doi.org/10.1029/2018JA025423

Vignes, D., M.H. Acuña, J.E.P. Connerney, D.H. Crider, H. Rème, and C. Mazelle (2002), Factors controlling the location of the Bow Shock at Mars, *Geophysical Research Letters*, Vol. 29, No. 9, 1328. doi:10.1029/2001GL014513

Table 1. The parameters used for all simulation runs.

Name	Symbol	value	unit
Inner boundary radius	R	3540	km
Solar wind number density	n_{sw}	2.4	cm^{-3}
Solar wind velocity	u_{sw}	350	km/s
Solar wind temperature	T_{sw}	$1.2 \cdot 10^5$	K
Solar wind magnetic field	$\mathbf{B}_{sw}$	$(-1, -2.7, -1)$	nT
Plasma resistivity	η	$5 \cdot 10^4$	Ω m
Obstacle resistivity		$7 \cdot 10^5$	Ω m
Particles per cell		128	
Weight of ionospheric ions		$2.2 \cdot 10^{21}$	
Height of max production	h_0	500	km
Atmospheric scale height	H	250	km
Cell size	Δx	350	km
Time step	Δt	0.05	s

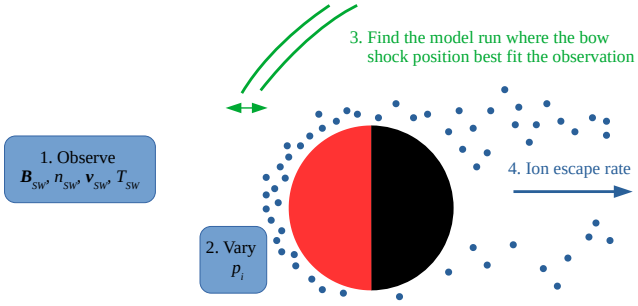

Figure 1. An illustration of the algorithm to estimate the ion escape rate. The Sun is to the left and Mars is the red and black disk. Using fixed upstream solar wind conditions from observations in the hybrid model, we vary the ionospheric heavy ion (blue dots) production rate for different simulation runs. The bow shock location (green lines) in each simulation run is then compared to the observed bow shock location. The estimated escape rate will then correspond to that of the simulation run that best fit the bow shock location.

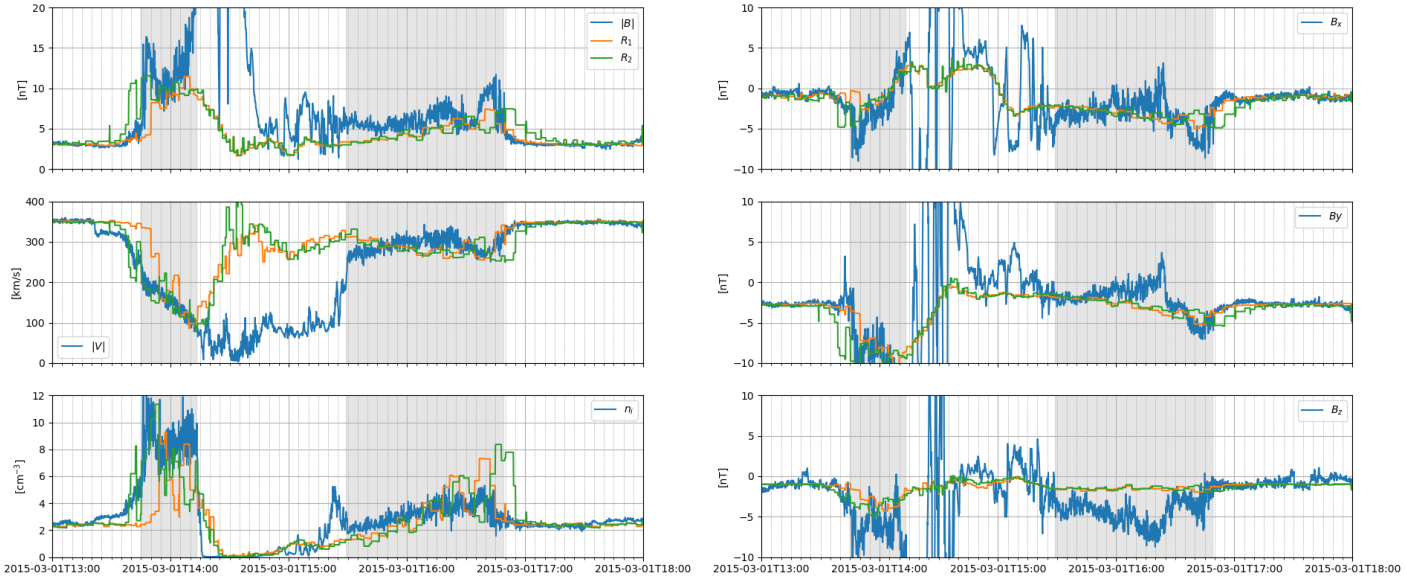

Figure 2. A comparison of MAVEN observations (blue) with two O^+ model runs (R_1 in orange and R_2 in green) at 490 s. In the left column, from the top, we have magnetic field magnitude, proton velocity, and proton number density. In the right column we have the three magnetic field components (B_x, B_y, and B_z) in MSO coordinates. Indicated in gray is also the location of the magnetosheath as seen from the observations. The induced magnetosphere is thus between the two gray regions.

Table 2. The different best fit simulation runs, the ionospheric ion specie, the maximum ionospheric production rates, and the resulting escape rates.

Run	1	2	3	4
Ionospheric specie	O^+	O^+	O_2^+	O_2^+
Production Rate, p_i [$cm^{-3}s^{-1}$]	0.4	0.5	0.4	0.5
Escape Rate [$10^{24}s^{-1}$]	1.985	1.989	1.452	1.463

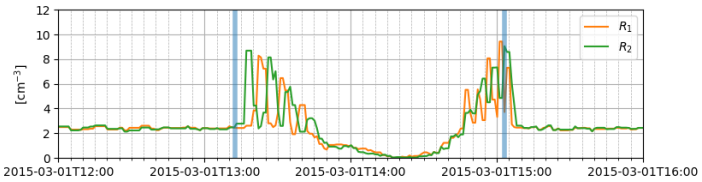

Figure 3. The proton number density along the MEX orbit for the two best fit simulation runs (R_1 in orange and R_2 in green), at 490 seconds of simulation time. The blue vertical lines show the two bow shock crossings seen in MEX electron data.